High-resolution dual comb spectroscopy using a free-running, bidirectional ring titanium sapphire laser

Sandrine Galtier, Clément Pivard, Jérôme Morville, Patrick Rairoux

Research Article | Vol. 30, No. 12 / 6 Jun 2022 / Optics Express 21148
Optics EXPRESS

High-resolution dual comb spectroscopy using a free-running, bidirectional ring titanium sapphire laser

SANDRINE GALTIER,* CLÉMENT PIVARD, JÉRÔME MORVILLE, AND PATRICK RAIROUX

Université de Lyon, Université Claude Bernard Lyon 1, CNRS, Institut Lumiére Matiére, F- 69622, Villeurbanne, France
**sandrine.galtier@univ-lyon1.fr*

Abstract: We report the first measurement of resolved molecular absorption lines with dual-comb spectroscopy using a Kerr-lens mode-locked bidirectional Ti:sapphire ring laser cavity. A 3 nm broad spectrum has been recorded in 5.3 ms with a spectral resolution of ≈ 1 GHz (0.05 cm-1) corresponding to a relative spectral resolution of 2.5×10^{-6}. The measurement of spectrally resolved molecular absorption lines have been demonstrated on the oxygen *A*-band at 394 THz (760 nm, 13 000 cm^{-1}) and was obtained with two free-running 100 fs Ti:sapphire trains of pulses without the need for active phase stabilization protocol nor real-time or post-processing correction. This work demonstrates that the bidirectional laser configuration enables a sufficient level of absolute and mutual coherence for dual-comb spectroscopy of resolved molecular absorption lines. Considering the high versatility of Ti:sapphire emission spectral range (from 600 to 1100 nm) with high-peak powers, the here reported results pave the way for Dual-Comb spectroscopy in the UV range at mW average output power using a standalone set-up, in the aim to extend its applicability for atmospheric remote-sensing.

1. Introduction

Dual comb spectroscopy (DCS) is an emerging spectroscopy technique with demonstrated applications from molecular metrology studies in laboratory [1,2] to open-path monitoring of atmospheric trace gases, as recently reviewed [3]. DCS differs from other well-known spectroscopy techniques as Fourier transform infrared spectroscopy (FTIR), grating spectrometer or scanning continuous wave (cw) laser spectroscopy, by combining a very fast acquisition duty cycle (down to tens of microsecond duty cycle) with state-of-the-art frequency resolution and accuracy that can be obtained within a wide spectral coverage. Compared to other laser comb-based techniques, DCS has been implemented in open-path measurements for high-resolution and broadband measurements. Indeed, DCS reveals its full potential when fast events have to be monitored or in turbulent environment such as atmospheric open-path applications. Open-path DCS can be implemented in a Long path absorption LIDAR (light detection and ranging) type experiment (LP-LIDAR). Very few research groups [3] have pushed the DCS technique from laboratory studies to *in-situ* atmospheric monitoring. This is due to the need of two laser sources with a high level of mutual coherence that must go hand-in-hand with sufficiently high radiation power, considering the power uptake of the atmospheric scattering and absorption in the chosen spectral range. Open-path DCS has so far be reported in the near-infrared range, at the maximum of emission of Erbium lasers [4–7] and in the mid-infrared using a QCL laser [8].

Performing open-path DCS in the UV region would be of particular interest for the observation of the physico-chemical processes involved in the atmosphere. The most reactive molecules of the atmosphere absorb in this spectral region, such as atmospheric radicals (OH, BrO, ClO$\cdots$). We recently showed in a simulation study [9], that a UV-DCS spectrometer based on Ti:sapphire

#455963 https://doi.org/10.1364/OE.455963
Journal © 2022 Received 15 Feb 2022; revised 9 May 2022; accepted 11 May 2022; published 31 May 2022

Optics EXPRESS

(TiSa) frequency comb lasers can achieve sufficient performance in terms of sensitivity to detect atmospheric UV absorbing molecules thanks to the sufficiently low phase noise and high power level of TiSa laser sources. Moreover, the TiSa technology presents a high versatile spectral coverage, from 600 to 1100 nm with efficient second or third harmonic generation, making it a very promising technology for multi-species monitoring. The deployment of UV-DCS as a remote sensing instrument depends on strict specifications: robustness (reliability), compactness and cost-efficient. When addressing the most reactive species of the atmosphere (atmospheric radicals) using optical spectroscopy, a high-resolution ($\leq$1 GHz) is also required for the evaluation of the interfering species. Different implementations have been reported to decrease the level of technological complexity and financial costs [10]. It is the case of dual-comb systems based on free-running laser sources generated from a single laser cavity. This particular implementation has the advantage of offering the highest output powers. A high level of mutual coherence has been reported using this laser configuration as phase and amplitude noise induced by the laser cavity length, pump laser and refractive index fluctuations are shared by the two trains of pulses.

Different architectures were demonstrated for free-running single cavity DCS: in mode-locked fiber lasers (via dual-wavelength multiplexing [11,12] or bidirectional emission [13,14]), in MIXSEL semiconductor lasers (via polarisation multiplexing [15,16]), in thin-disk lasers (via spatial multiplexing [17] and polarisation multiplexing [18]) and in a solid-state lasers via polarisation multiplexing [19,20]. The unique demonstration of free-running and single cavity DCS using a Ti:sapphire solid-state laser has been reported by Idegushi *et al* [21], and via bidirectional emission in a ring-cavity. They report Dual-comb absorption spectroscopy of a Nd:YVO_4 crystal with a resolution of 93 GHz.

We here report DCS measurements at the GHz resolution level by using a Ti:Sa bi-directional Kerr-lens mode-locked (KLM) ring laser which corresponds to two orders of magnitude resolution enhancement compared to the previous quoted work. We first describe the development of our home-made bidirectional DC spectrometer (BD-DCS), and the laser system inspired from the work of Garduno-Mejia [22] which differs from the work of Idegushi *et al* in cavity (arrangement and length), crystal length and intra-cavity dispersion management. We then present measurement results using DCS on a Fabry Perot etalon and on the O_2-A absorption band of oxygen in an open-path configuration. Despite the raw nature of the presented DCS measurements (no averaging nor phase correction), the achieved resolution allows for the observation of the line-resolved molecular absorption spectrum in a broad spectral range. We finally discuss on the achieved quality factor of the presented DCS measurements.

2. DC spectrometer implementation

2.1. Principle of DCS

Dual-comb spectroscopy is based on a multi-heterodyne beating of two mutually coherent frequency combs, allowing to down-convert the optical frequencies into the radio-frequency (RF) domain. Frequency combs have been extensively described in the literature [23]. Their spectrum is composed of equidistant "comb lines" of frequency $f_o + n \times f_{rep}$, where n is an integer, f_{rep} the repetition rate of the laser pulses, and the offset frequency f_o which accounts for the velocity difference between the carrier and the envelope of the pulses. For dual-comb spectroscopy, each laser source must present a comb structure with slightly different repetition rate $\Delta f_{rep} = f_{rep2} - f_{rep1}$, that creates a time dependant optical path difference between the two trains of pulses. When both beams are superimposed, their interference is detected on a single photodiode, producing a temporal interferogram (IGM). The application of Fourier transform on the IGM reveals a RF comb structure imprinted by eventual molecular absorption features. The frequencies of the RF "comb lines" are worth $\Delta f_o + k \times \Delta f_{rep}$ where k is an integer and $\Delta f_o = f_{o2} - f_{o1}$ is the differential carrier-envelop offset frequency. Considering a DCS description in the frequency domain, the slight repetition rate difference Δf_{rep} is the source of the RF beat

Optics EXPRESS

notes: the comb lines of laser 1 beating with the comb lines of laser 2. The use of a low pass filter, after photodetection, selects the beat note that occurs between the closest comb lines from each laser corresponding to the lowest order of the RF beat-notes. From the RF spectrum, the optical spectrum can be retrieved using the up-scaling mapping factor $a = \frac{f_{rep}}{\Delta f_{rep}}$, Δf_o and f_{o1} or f_{o2}. Exhaustive presentations of the DCS principle can be found in recent reviews [24,25].

The here presented dual-comb system makes use of two coherent light beams generated from an unique ring laser cavity in which the two beams propagate in opposite directions (see Fig. 1). The beam transmitted through the output coupler (OC) and right after the P4 prism is called *dir1* whereas the beam reflected by the M3 mirror before the OC is called *dir2*. Those two laser beams are combined using a 50/50 beamsplitter, and focused onto a Si-photodetector after free-space propagation. The generated photo-current is amplified using a transimpedance amplifer (DHPCA-100 - BW 80 MHz from Femto) and the signal is filtered using a low pass filter with a cut-frequency of 50 MHz (PLP-50+ from Minicircuit). The signal is digitized by an A/D fast acquisition card (M4i.4450-x8, 14 bit transient recorder from Spectrum) with an acquisition rate of 125 MHz. The low pass filter prevents aliasing and selects the lowest order of RF beat-note frequencies as discussed before. We first present below the specifications of the two generated laser beams before presenting broadband and high-resolution measurements with our set up in section 3.

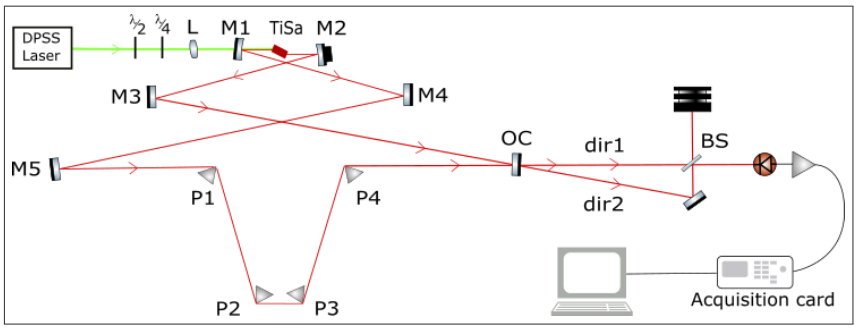

Fig. 1. Dual-comb spectrometer set-up using a home-made bidirectional Ti:sapphire ring laser. The polarisation of the diode-pumped solid-state (DPSS) green pump laser is adjusted by the use of half ($\lambda/2$) and quarter ($\lambda/4$) wave-plates. The pump laser beam (green line) is focused into the TiSa crystal via a 100 mm radius of curvature convex lens (L) . The laser cavity is composed of two curved mirrors of 50 mm focal distance (M1 and M2), three plane mirrors (M3, M4, M5), four SF10 prisms (P1-4) and a wedged 90% reflective output coupler (OC). The two laser beam directions of emission are overlapped using a beam-splitter (BS). The beam is directed into a photodiode (PD), the photocurrent is amplified and low-pass filtered before digitization using an A/D acquisition card.

2.2. Bidirectional ring laser cavity

The geometry of the Ti:Sa cavity is illustrated in Fig. 1. The optical resonator consists in a six-mirrors bow-tie ring cavity configuration with two concave mirrors (M1, M2) with 100 mm radius of curvature (R=99.8 %), three plan mirrors (R = 99.9 %) and a wedged output coupler (R = 90%). The 10 mm long Ti:Sa crystal is pumped by a diode-pumped solid-state laser at 532 nm with an average power of approximately 5.5 W. A set of four SF10 prisms (P1-4) is used for dispersion management (similar arrangement can be found in [22]). The laser emits up to 1 W total average power in continuous-wave (cw) mode. The soft-aperture Kerr-lens modelocking (KLM) operation is triggered by a manual perturbation on the common translation stage shared by P2 and P3 prisms. The laser can emit either unidirectionally, or bidirectionally with KLM

Optics EXPRESS

in only one direction and cw in the other direction or KLM in both directions. The different regimes of operation are triggered using different M1-M2 distances, and different alignments of the cavity mirrors.

Stable bidirectional KLM operation has been obtained at the center of the cavity stability zone for the cw operation. It is then maintained without any interruption by translating the M2 mirror over a range of 1 mm. Typical output powers are ≈300 mW in both directions resulting in ≈600 mW in total with repetition rates of both combs in the range of 118 MHz.

The repetition rate of one comb compared to the other can be tuned by adjusting the prisms insertion, the position of the pump lens or the tilt of one of the plane mirrors. A similar dependence of Δf_{rep} values with the cavity element positioning has been reported in [21]. With our set-up, Δf_{rep} values from 0 to 450 Hz have been achieved. Examples of output spectra, measured using a commercial grating spectrometer (AvaSpec-ULS3648 - 1 nm resolution - AVANTES), are presented in Fig. 2. For low Δf_{rep} values ($\leq$ 100 Hz), the output spectra of both emissions nicely superimpose but a subsequent difference in shape and central position is observed the higher the Δf_{rep} value.

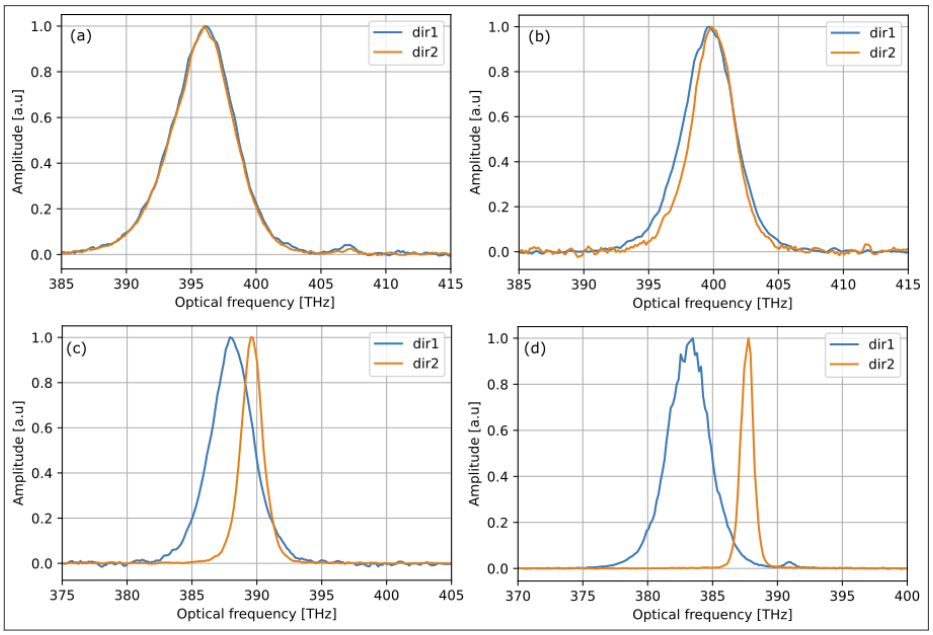

Fig. 2. Normalized spectra of the two laser beams (*dir1* and *dir2*), measured with a grating-based spectrometer for different Δf_{rep} values: 1.2 Hz (a), 10.4 Hz (b) 107 Hz (c) and 425 Hz (d).

We measured the duration of the laser pulses using a commercial interferometric autocorrelator and obtained typical values from 70 to 100 femtoseconds depending on the prisms insertion. These specifications allow for efficient harmonic generation in bulk crystals (second or third harmonic generation) and therefore for the possibility of carrying out dual-comb spectroscopy in the UV range.

3. Broadband and high-resolution DCS measurements

3.1. Spectral envelop retrieval

In this section, we present a DCS measurement of the overlap between the two output spectra and compare it with the grating-based spectrometer measure of their individual spectrum. This

Optics EXPRESS

requires the knowledge of the mapping factor $a = f_{rep}/\Delta f_{rep}$. We present here the methodology used to determine Δf_{rep} and f_{rep}.

Figure 3(a) shows the temporal trace of nine successive recorded IGMs. The nine short and intense signal bursts are created when the pulses of both lasers overlap in time at the detector, such events are called "centerbursts". Because the value of f_{o1} and f_{o2} are not both worth zero, we observe a variation in time of the centerbursts amplitude. We also observe a small prompt lost of power followed by an exponential-like recovery pattern, that occurs between two centerbursts. We attribute this perturbation to a laser gain depletion effect when both laser pulses overlap inside the Ti:Sa crystal. This assumption is corroborated by the fact that the time delay between the start of this perturbation and the following centerburst matches the one between the moment when the pulses meet inside the Ti:Sa crystal and when they meet (and are superimposed) at the beam-splitter. Further investigations are needed to precisely quantify this observation.

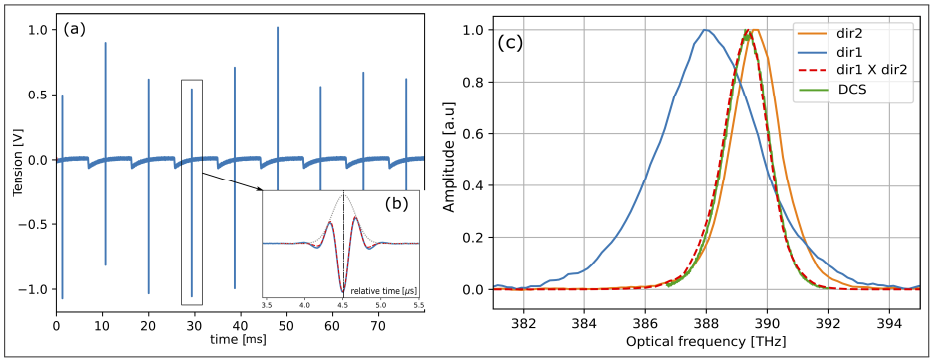

Fig. 3. (a) Typical DCS temporal trace with $\Delta f_{rep} \approx 107$ Hz and $f_{rep} \approx 118$ MHz. (b) Zoom on a centerburst (blue), fitted with an oscillating function (red) multiplied by a Gaussian envelop (grey dotted). The dot-dash vertical line indicates the center of the Gaussian envelop. The IGMs are over-sampled at a rate of 125 MHz. (c) The normalized DCS spectrum obtained from the FFT of the temporal trace of (b) (green) and normalized spectra of both laser outputs measured using a grating spectrometer (blue and orange). The DCS spectrum overlaps with the product of the spectral power density of both emissions (red dashed). The central position of the DCS spectrum has been adjusted using the free parameter Δf_o.

The time delay between two centerbursts is $1/\Delta f_{rep}$. We estimate Δf_{rep} by fitting each centerburst with an oscillating function with a fixed carrier frequency and a Gaussian envelop (see Fig. 3(b)). The center position of the Gaussian envelop gives the time position of the centerburst. A linear fit to the centerburst number as function of its time position is then applied. From the slope, we extract the Δf_{rep} value. A ten mHz uncertainty is deduced from the standard deviation of the residuals. f_{rep2} is extracted from numerical Fast Fourier Transform (FFT) using a sampling frequency of 250 MHz on the temporal signal of *dir 2*. This allows a minimum Fourier-bandwidth limited precision of $\approx$ 10 Hz- limited by the A/D card memory.

A RF spectrum is then obtained via FFT of a single centerbust. The determination of the mapping factor a gives access to the optical frequencies grid (the spectral elements spacing). The absolute position of the optical frequencies requires the knowledge of the offset frequency value of one of the FC and the differential offset frequency Δf_o. Fully referenced FCs are therefore required [1,2]. In this work, the laser sources are free-running and two different strategies are used to retrieve the absolute optical frequencies: 1) a coarse determination is done using a conventional grating-based spectrometer calibrated on known atomic lines to retrieve Δf_o, 2) by a direct comparison with known molecular absorption lines tabulated in spectroscopic data bases.

Optics EXPRESS

From the data of Fig. 3(a), we extract a Δf_{rep} value of 107.11(3) Hz. The a factor is then $11043(3)\times10^2$. Considering the relative uncertainty on Δf_{rep} and f_{rep}, the precision of the a factor is limited by the Δf_{rep} uncertainty only. After the up-scaling with the mapping factor, we adjust Δf_o to make coincide the DCS spectrum with the spectrum corresponding to the multiplication of the two laser spectra measured with a grating-based spectrometer. With a 1.0 nm resolution grating spectrometer (500 GHz at 800 nm), Δf_o can be retrieved with 0.5 MHz uncertaincy. As illustrated in Fig. 3(c), the width of the DCS spectrum agrees well with the one expected from the measured laser output spectra. This validates the determination of the mapping factor value within the resolution of this measurement. It is worth noting that the retrieval of the envelop spectrum does not need a high resolution DCS measurement. The temporal window used to calculate the DCS spectra is ≈ 2 μs which translates into an instrumental spectral resolution of $\approx$ 550 GHz (a /2 μs).

3.2. Fabry-Perot spectroscopy

To further investigate the validity of the mapping factor value, we perform DCS using a Fabry-Perot (FP) etalon. The measurement was done in a symmetric geometry (both trains of pulses are transmitted through the etalon) to optimize the signal-to-noise ratio (SNR). Figure 4(a) shows a 100 μs boxcar truncation of the temporal trace and its corresponding FFT. The smaller echos from either part of the centerburst come from the attenuated internal reflections of the FP etalon as revealed by the FP transmission function in the RF domain (see Fig. 4(b)). The repetition rate f_{rep2} and the differential repetition rate Δf_{rep} are necessary and sufficient to extract the experimental free spectral range (FSR) of the FP etalon. The Δf_{rep} value of 107.691(6) Hz is extracted from the analysis of nine subsequent IGMs and f_{rep2} is worth 118.2857(25) MHz with no need to improve its precision. The mapping a factor is then $1,093,677(66)$. The FSR evaluation requires a relative frequency knowledge only and not an absolute mapping between the RF and optical frequencies. However, the RF frequencies are translated into optical frequencies according to the previous presented method for convenience. Figure 4(c) shows the optical spectrum normalized by its envelop. The result of a fit using the FP etalon transmission function, with the FSR as a free parameter, is also shown superimposed to the data. From this, we determine a FSR value of 73.740 GHz. This commercial etalon is specified to have a finesse of ≈ 3 and a FSR of 75(1) GHz. The difference with the constructor value is consistent with its nominal uncertainty and the slight tilt of the etalon we introduced to avoid optical feedback.

The statistical uncertainty on the FSR value depends on both the SNR and the a factor uncertainty. The uncertainty due to the SNR is extracted from the Jacobian matrix of the least-square fitting algorithm and is worth ≈ 5 MHz. The a factor relative uncertainty is 6×10^{-5} and translates into 4 MHz for the FSR value. Their combination gives a global uncertainty between 6 and 9 MHz depending on the degree of correlation. However, by applying the same treatment over the 9 subsequent interferograms, we observe a dispersion of the FSR values with a standard deviation of 100 MHz. The source of this dispersion is not yet understood but a beam pointing instability may explain a part of it and will be investigated via a thorough characterization of the laser beam and the light collection system. Finally, this measurement validates, via the achieved statistical precision on individual FSR value, the a factor statistical uncertainty determined *a posteriori* by the previous presented methodology.

3.3. High-resolution measurement using O_2 absorption spectrum

We evaluate the potential of our system to be applied for open-path atmospheric spectroscopy using the A-band of ambient oxygen. The DCS system is set in a symmetric geometry where both pulse trains propagate collinearly over an absorption path of 7 meters. The path length together with the two times signal enhancement due to the symmetric geometry, allow to identify these doubly forbidden $b^1\Sigma_g^+ - X^3\Sigma_g^-$ electronic transitions of oxygen. Figure 5(a) shows an example

Optics EXPRESS

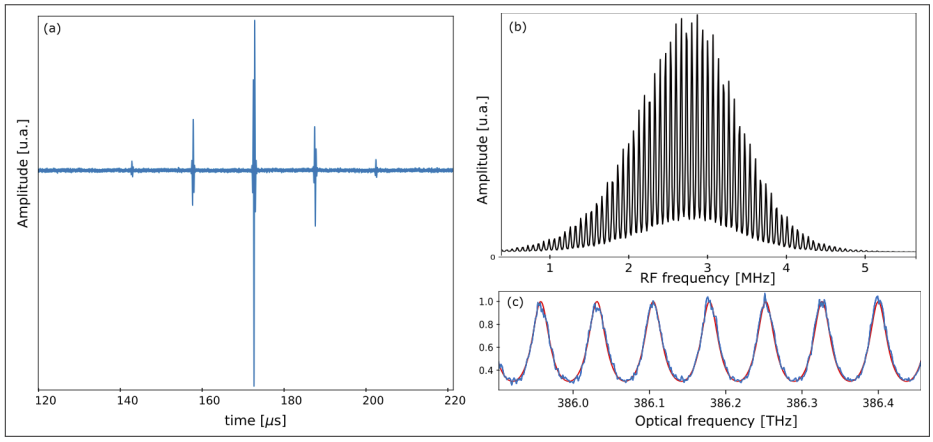

Fig. 4. DCS results on a FP transmission function.(a) Temporal interferometric trace (b) spectrum obtained from the FFT of the interferogram trace showing the expected convolution between the spectral laser envelop and the transmission of a Fabry-Perot etalon. (c) Zoom of the spectrum (blue) rescaled in the optical domain fitted with the simulated transmission expression (red) of a FP etalon.

of a retrieved spectrum from one interferogram. The temporal window on which the FFT was performed has been chosen as a compromise between both the resolution and the SNR. Using a boxcar temporal window of 5.3 ms, the theoretical experimental line-width is 700 MHz (full width half-max of the sinc function). On the left side of the spectrum, the R band of the $O_2 - A$ absorption band is visible.

The up-conversion to the optical domain is done first by determining the mapping factor a using $\Delta f_{rep} = 19.97(4)$ Hz and $f_{rep2} \approx 118$ MHz. A coarse estimation of the baseline using a Tchebychev polynomial over the full envelop spectrum enables to normalize the RF spectrum from which the absorption lines centers are deduced using a peak and level-crossing algorithm based on a sweeping Gaussian protocol written for Igor Pro (WaveMetrics^{TM}). The absolute frequencies are then determined by identification of the more intense R8Q7 molecular line position with the corresponding HITRAN line position which includes the atmospheric pressure shift [26]. Figure 5(b) shows the unambiguous identification of the transitions.

To evaluate the spectral resolution of the measured spectrum, Fig. 5(c) shows an overlap of the measured R12Q11 and R13R13 O_2 absorption lines with a simulated HITRAN spectrum using the natural abundance of oxygen at a pressure of 1 atmosphere and a temperature of 296°K. The simulated line profiles are computed with a Voigt line-shape function convoluted with the sinc instrumental line shape function. The half width at half maximum of the pressure-broadened absorption line at those conditions is 1.5 GHz and the effect of the convolution is negligible considering the instrumental line-width. The agreement between the measured and simulated spectra demonstrates an achieved resolution of 1.5 GHz. This result indicates a sufficient stability of Δf_{rep} and Δf_o over the 5.3 ms time windows, and therefore a sufficient absolute and mutual coherence of the two generated trains of pulse, for spectrally resolved measurements at the GHz resolution level. This result is 2 orders of magnitude better than the previous reported system using a co-propagating free-running TiSa lasers [19].

The agreement of the overlap shown in Fig. 5(c) can also be used to evaluate the SNR of the molecular spectrum. This is done by subtracting the HITRAN spectrum from the measured one and by calculating the standard deviation of the result. A standard deviation of 0.055 is obtained which gives an SNR for the R12Q11 and R13R13 lines of around 5, using an absorption depth of

Optics EXPRESS

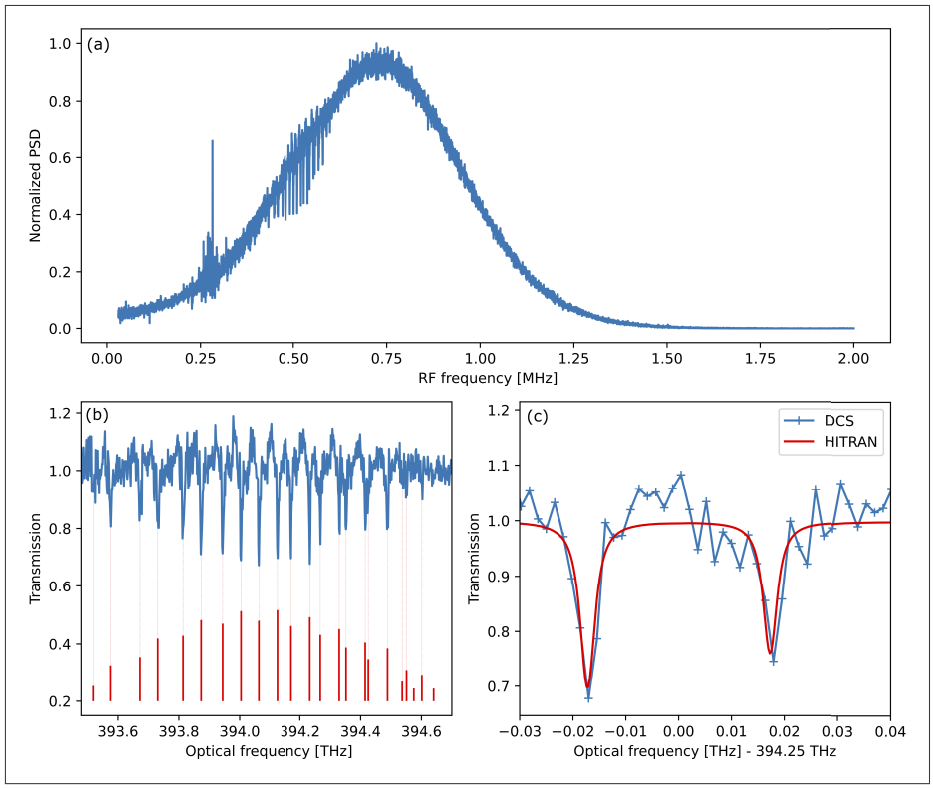

Fig. 5. (a) DCS normalized power spectral density (PSD) measured after 7 meters of light propagation through air. The peaks at 0.25 MHz are due to electronic noise. (b) A zoom of the observed O_2 absorption line (baseline removed) with frequency scale converted to optical frequency. The expected line position (HITRAN database) are shown for visual identification [26]. (c) Overlap between the R12D11 and R13R13 O_2 absorption lines with a simulated HITRAN spectrum using the natural abundance of oxygen at a pressure of 1 atmosphere and a temperature of 296°K.

0.3. Because of the limited SNR on the absorption lines, we decided to focus the discussion on the spectral resolution of the experiment. However this treatment demonstrates an agreement between the expected O_2 concentration within the estimated 20% uncertainty.

4. Discussion

This work shows that the bidirectional cavity geometry guarantees a sufficient absolute and mutual coherence for GHz resolution level in the near-IR domain. In order to compare the sensitivity of our measurement with the literature values, we evaluate the quality factor Q, defined as SNR(ν) $\times M/\sqrt{T}$ where M is the number of spectral element and T the acquisition time [27]. The spectral SNR(ν) is determined as follows: the spectrum is normalized with the base-line function leading to the definition of the SNR as $1/\sigma(\nu)$ where $\sigma(\nu)$ is the standard deviation of the baseline-flattened spectrum over regions with no detectable absorption. Using the data of Fig. 5(a), the spectral SNR is 77 at the top of the envelop and 50 in average. The data spans 6 THz and the spectral point spacing is 1.16 GHz (a/5.3ms) resulting in M = 5172 spectral elements. The quality factor is therefore 3.5×10^6 Hz$^{1/2}$ (5.5×10^6 Hz$^{1/2}$ at maximum SNR). This value is of the same order of magnitude than the state-of-the-art value using single-cavity

Optics EXPRESS

dual-comb spectroscopy in the near-infrared [28]. However, this extrapolation at the time scale to the second, relies on the purely white nature of the noise and on the implementation of efficient averaging protocols. As a first step, we implemented the Forman-Vanasse phase correction on the FP and O_2 spectra to correct for Δf_o fluctuations, as described previously on DCS IGMs [17]. By averaging seven consecutive corrected interferograms, the SNR of the resulting averaged spectrum is increased by a factor ≈2.2, consistent with the 2.6 expected value, taking into account the statistical uncertainty due to the low number of averaged spectra. To reach longer averaging time, real-time adaptive sampling [29], real-time computational correction [30] or feed-forward control [31] can be implemented by the use of auxiliary cw narrow line-width lasers. The mutual coherence of the combs can also be reconstructed using self-referencing correction algorithms, without any extra measurements or optical elements [28,32–35]. This will also improve the SNR nominal value.

5. Conclusion

We have presented a dual comb architecture based on a bidirectional ring-laser cavity generating two kerr-lens mode-locked trains of pulses. The differential repetition rate of these two free-running frequency combs has been tuned from Δf_{rep} = 0 Hz to 450 Hz. Thanks to this setup, DCS has been performed at different time windows, from 2 μs to few milliseconds and a FP etalon was used to validate the radio-frequency to optical frequency mapping. Dual-comb spectra of resolved molecular lines have been presented indicating a sufficient absolute and mutual coherence of the two generated trains of pulses for 1.5 GHz resolution measurements. This intrinsic relative coherence is reported without any active phase stabilisation protocols nor phase correction protocols. Up to our knowledge, this paper reports the best spectral resolution achieved for a Dual Comb spectroscopy with free running TiSa lasers, with a resolution improvement of two orders of magnitude compared to the literature [21,36].

The generated high total output power (600 mW) with 100 fs pulse duration and 6 THz spectral span, suggest promising applications in the UV range. Milliwatt level power in the UV is indeed a prerequisite for long-path LIDAR on UV absorbing trace gases detection [9]. For the applicability of DCS for remote-sensing in the UV range, the implementation of efficient averaging protocols are a perquisite. Phase correction protocols will be deployed in this aim.

Funding. Université Claude Bernard Lyon 1 (FRAMA); Institut de Physique (EMERGENCE).

Acknowledgments. We thank Pr. Jesús Garduño-Mejia and Dr. Ramirez Catalina (Instituto de Ciencias aplicadas y Tecnologia - UNAM University) for their help in designing the bidirectional ring laser cavity. We also want to thank our colleagues from ILM for providing a green pump laser at different stages of the project. We finally thank the anonymous reviewers for their contribution in improving the discussion.

Disclosures. The authors declare no conflicts of interest.

Data availability. Data underlying the results presented in this paper are not publicly available at this time but may be obtained from the authors upon request.

References

1. B. Bernhardt, A. Ozawa, P. Jacquet, M. Jacquey, Y. Kobayashi, T. Udem, R. Holzwarth, G. Guelachvili, T. W. Hänsch, and N. Picqué, "Cavity-enhanced dual-comb spectroscopy," Nat. Photonics **4**(1), 55–57 (2010).
2. N. Hoghooghi, R. J. Wright, A. S. Makowiecki, W. C. Swann, E. M. Waxman, I. Coddington, and G. B. Rieker, "Broadband coherent cavity-enhanced dual-comb spectroscopy," Optica **6**(1), 28–33 (2019).
3. K. C. Cossel, E. M. Waxman, E. Baumann, F. R. Giorgetta, S. C. Coburn, C. B. Alden, and B. R. Washburn, "2 - remote sensing using open-path dual-comb spectroscopy," in *Advances in Spectroscopic Monitoring of the Atmosphere*, W. Chen, D. S. Venables, and M. W. Sigrist, eds. (Elsevier, 2021), pp. 27–93.
4. G. B. Rieker, F. R. Giorgetta, W. C. Swann, J. Kofler, A. M. Zolot, L. C. Sinclair, E. Baumann, C. Cromer, G. Petron, C. Sweeney, P. P. Tans, I. Coddington, and N. R. Newbury, "Frequency-comb-based remote sensing of greenhouse gases over kilometer air paths," Optica **1**(5), 290–298 (2014).
5. S. Coburn, C. B. Alden, R. Wright, K. Cossel, E. Baumann, G.-W. Truong, F. Giorgetta, C. Sweeney, N. R. Newbury, K. Prasad, I. Coddington, and G. B. Rieker, "Regional trace-gas source attribution using a field-deployed dual frequency comb spectrometer," Optica **5**(4), 320–327 (2018).

Optics EXPRESS

6. D. Herman, C. Weerasekara, L. Hutcherson, F. Giorgetta, K. Cossel, E. Waxman, G. Colacion, N. Newbury, S. Welch, B. DePaola, I. Coddington, E. Santos, and B. Washburn, "Precise multispecies agricultural gas flux determined using broadband open-path dual-comb spectroscopy," Sci. Adv. **7**(14), eabe9765 (2021).
7. J. Oudin, A. K. Mohamed, and P.-J. Hébert, "IPDA LIDAR measurements on atmospheric CO2 and H2O using dual comb spectroscopy," in *International Conference on Space Optics – ICSO 2018*, vol. 11180 Z. Sodnik, N. Karafolas, and B. Cugny, eds., International Society for Optics and Photonics (SPIE, 2019), pp. 1018–1024.
8. J. Macarthur, J. Hayden, M. S. Warden, C. Carson, D. M. Stothard, and V. G. Savitski, "Dual-comb scanning spectrometer for remote sensing of traces of explosives," IEEE Trans. Instrum. Meas. **71**, 1–11 (2022).
9. S. Galtier, C. Pivard, and P. Rairoux, "Towards dcs in the uv spectral range for remote sensing of atmospheric trace gases," Remote Sens. **12**(20), 3444 (2020).
10. R. Liao, H. Tian, W. Liu, R. Li, Y. Song, and M. Hu, "Dual-comb generation from a single laser source: principles and spectroscopic applications towards mid-IR—a review," JPhys Photonics **2**(4), 042006 (2020).
11. X. Zhao, G. Hu, B. Zhao, C. Li, Y. Pan, Y. Liu, T. Yasui, and Z. Zheng, "Picometer-resolution dual-comb spectroscopy with a free-running fiber laser," Opt. Express **24**(19), 21833–21845 (2016).
12. J. Fellinger, A. S. Mayer, G. Winkler, W. Grosinger, G.-W. Truong, S. Droste, C. Li, C. M. Heyl, I. Hartl, and O. H. Heckl, "Tunable dual-comb from an all-polarization-maintaining single-cavity dual-color yb:fiber laser," Opt. Express **27**(20), 28062–28074 (2019).
13. S. Mehravar, R. A. Norwood, N. Peyghambarian, and K. Kieu, "Real-time dual-comb spectroscopy with a free-running bidirectionally mode-locked fiber laser," Appl. Phys. Lett. **108**(23), 231104 (2016).
14. Y. Nakajima, Y. Hata, and K. Minoshima, "High-coherence ultra-broadband bidirectional dual-comb fiber laser," Opt. Express **27**(5), 5931–5944 (2019).
15. S. M. Link, D. J. H. C. Maas, D. Waldburger, and U. Keller, "Dual-comb spectroscopy of water vapor with a free-running semiconductor disk laser," Science **356**(6343), 1164–1168 (2017).
16. J. Nürnberg, C. G. E. Alfieri, Z. Chen, D. Waldburger, N. Picqué, and U. Keller, "An unstabilized femtosecond semiconductor laser for dual-comb spectroscopy of acetylene," Opt. Express **27**(3), 3190–3199 (2019).
17. T. Hofer, K. Fritsch, N. Picqué, and O. Pronin, "Dual-comb thin-disk oscillator," arXiv:2004.10303 (2020).
18. N. Modsching, J. Drs, P. Brochard, J. Fischer, S. Schilt, V. J. Wittwer, and T. Südmeyer, "High-power dual-comb thin-disk laser oscillator for fast high-resolution spectroscopy," Opt. Express **29**(10), 15104–15113 (2021).
19. B. Willenberg, J. Pupeikis, L. M. Krüger, F. Koch, C. R. Phillips, and U. Keller, "Femtosecond dual-comb yb:caf2 laser from a single free-running polarization-multiplexed cavity for optical sampling applications," Opt. Express **28**(20), 30275–30288 (2020).
20. M. Kowalczyk, L. Sterczewski, X. Zhang, V. Petrov, Z. Wang, and J. Sotor, "Dual-comb femtosecond solid-state laser with inherent polarization-multiplexing," Laser Photonics Rev. **15**, 2000441 (2021).
21. T. Ideguchi, T. Nakamura, Y. Kobayashi, and K. Goda, "Kerr-lens mode-locked bidirectional dual-comb ring laser for broadband dual-comb spectroscopy," Optica **3**(7), 748–753 (2016).
22. J. Gardu no-Mejia, M. Mohebi, and N. Jamasbi, "The role of cavity design in a bi-directional kerr lens mode locked ring ti:sapphire laser," Opt. Commun. **207**(1-6), 307–314 (2002).
23. T. W. Hänsch, "Nobel lecture: Passion for precision," Rev. Mod. Phys. **78**(4), 1297–1309 (2006).
24. I. Coddington, N. Newbury, and W. Swann, "Dual-comb spectroscopy," Optica **3**(4), 414–426 (2016).
25. N. Picqué and T. W. Hänsch, "Frequency comb spectroscopy," Nat. Photonics **13**(3), 146–157 (2019).
26. I. Gordon, L. Rothman, R. Hargreaves, R. Hashemi, E. Karlovets, F. Skinner, E. Conway, C. Hill, R. Kochanov, Y. Tan, P. Wcislo, A. Finenko, K. Nelson, P. Bernath, M. Birk, V. Boudon, A. Campargue, K. Chance, A. Coustenis, B. Drouin, J. Flaud, R. Gamache, J. Hodges, D. Jacquemart, E. Mlawer, A. Nikitin, V. Perevalov, M. Rotger, J. Tennyson, G. Toon, H. Tran, V. Tyuterev, E. Adkins, A. Baker, A. Barbe, E. Cané, A. Császár, A. Dudaryonok, O. Egorov, A. Fleisher, H. Fleurbaey, A. Foltynowicz, T. Furtenbacher, J. Harrison, J. Hartmann, V. Horneman, X. Huang, T. Karman, J. Karns, S. Kassi, I. Kleiner, V. Kofman, F. Kwabia-Tchana, N. Lavrentieva, T. Lee, D. Long, A. Lukashevskaya, O. Lyulin, V. Makhnev, W. Matt, S. Massie, M. Melosso, S. Mikhailenko, D. Mondelain, H. Müller, O. Naumenko, A. Perrin, O. Polyansky, E. Raddaoui, P. Raston, Z. Reed, M. Rey, C. Richard, R. Tóbiás, I. Sadiek, D. Schwenke, E. Starikova, K. Sung, F. Tamassia, S. Tashkun, J. Vander Auwera, I. Vasilenko, A. Vigasin, G. Villanueva, B. Vispoel, G. Wagner, A. Yachmenev, and S. Yurchenko, "The HITRAN2020 molecular spectroscopic database," J. Quant. Spectrosc. Radiat. Transfer **277**, 107949 (2022).
27. N. R. Newbury, I. Coddington, and W. Swann, "Sensitivity of coherent dual-comb spectroscopy," Opt. Express **18**(8), 7929–7945 (2010).
28. L. A. Sterczewski, J. Westberg, and G. Wysocki, "Computational coherent averaging for free-running dual-comb spectroscopy," Opt. Express **27**(17), 23875–23893 (2019).
29. T. Ideguchi, A. Poisson, G. Guelachvili, N. Picqué, and T. W. Hänsch, "Adaptive real-time dual-comb spectroscopy," Nat. Commun. **5**(1), 3375 (2014).
30. J. Roy, J.-D. Deschênes, S. Potvin, and J. Genest, "Continuous real-time correction and averaging for frequency comb interferometry," Opt. Express **20**(20), 21932–21939 (2012).
31. Z. Chen, M. Yan, T. W. Hänsch, and N. Picqué, "A phase-stable dual-comb interferometer," Nat. Commun. **9**(1), 3035 (2018).
32. N. B. Hébert, J. Genest, J.-D. Deschênes, H. Bergeron, G. Y. Chen, C. Khurmi, and D. G. Lancaster, "Self-corrected chip-based dual-comb spectrometer," Opt. Express **25**(7), 8168–8179 (2017).

Optics EXPRESS

33. N. B. Hébert, M.-B. V J.-D. Deschênes, and J. Genest, "Self-correction limits in dual-comb interferometry," IEEE J. Quantum Electron. **55**(4), 1–11 (2019).
34. H. Yu, K. Ni, Q. Zhou, X. Li, X. Wang, and G. Wu, "Digital error correction of dual-comb interferometer without external optical referencing information," Opt. Express **27**(20), 29425–29438 (2019).
35. D. Burghoff, N. Han, and J. H. Shin, "Generalized method for the computational phase correction of arbitrary dual comb signals," Opt. Lett. **44**(12), 2966–2969 (2019).
36. A. Schliesser, M. Brehm, F. Keilmann, and D. W. van der Weide, "Frequency-comb infrared spectrometer for rapid, remote chemical sensing," Opt. Express **13**(22), 9029–9038 (2005).